RSC Advances

ROYAL SOCIETY OF CHEMISTRY

PAPER

View Article Online
View Journal | View Issue

Cite this: *RSC Adv.*, 2026, **16**, 20514

Preparation of amorphous calcium phosphate nanoparticles using small organic molecules for biomimetic mineralization of dentin

Zhenni Liu,[a] Dan Li,[a] Xiujun Shi,[a] Dongqin Xiao,[a] Feng Shi,[b] Xuwei Luo,[a] Gang Feng,[a] Yonglin Xie*[a] and Chengdong Zhang*[a]

Received 31st December 2025
Accepted 20th March 2026

DOI: 10.1039/d5ra10131j

rsc.li/rsc-advances

The development of nanomaterials capable of effectively occluding dentinal tubules and inducing biomimetic mineralization is critical for treating dentin hypersensitivity and early-stage caries. Owing to its high reactivity, amorphous calcium phosphate (ACP) serves as an ideal mineralization precursor. Although organic molecules are known to modulate and stabilize ACP, how small organic molecules (SOM) with distinct functional groups influence its remineralization efficacy remains incompletely understood. In this work, phytic acid (IP6) and cyclohexanehexacarboxylic acid (H6L), two structurally analogous yet functionally distinct molecules, were used as regulators to synthesize organic/ACP nanocomposites, denoted as IP6/CaP and H6L/CaP, respectively. A control sample prepared without organic additives was denoted as CaP. These composites were systematically evaluated for their ability to occlude dentinal tubules, promote remineralization, and resist acid challenge, using commercial 45S5 bioactive glass (BG) as a positive control. Material characterization revealed that the CaP comprised hydroxyapatite with an average particle size of 548.75 ± 2.32 nm. In contrast, both IP6 and H6L facilitated the formation of uniformly distributed microscale round-shaped aggregates, yielding IP6/CaP and H6L/CaP with average diameters of 87.64 ± 2.37 nm and 99.56 ± 1.67 nm, respectively. *In vitro* mineralization assays showed that IP6/CaP induced a uniform, dense nanomineral layer on both the dentin surface and type I collagen, achieving optimal integration within the collagen matrix. H6L/CaP led to the formation of uniformly distributed microscale round-shaped aggregates, whereas CaP produced disordered, loosely packed large crystals, indicative of poor mineralization quality. Dentinal tubule occlusion tests demonstrated that IP6/CaP and H6L/CaP afforded significantly superior sealing and acid resistance compared to both CaP and BG. Cytotoxicity assays confirmed the good biocompatibility of all materials. In summary, both IP6 and H6L effectively stabilized ACP and inhibited its phase transformation to hydroxyapatite. Notably, IP6/CaP outperformed both CaP and H6L/CaP in dentin remineralization and tubule occlusion, providing valuable guidance for the rational design of next-generation materials for dental desensitization and hard tissue regeneration.

Introduction

With the aging population and shifts in dietary patterns, dental caries and dentin hypersensitivity, resulting from demineralization of dental hard tissues, have become major public health challenges worldwide.[1,2] Mainstream "replacement" therapies (*e.g.*, resin fillings, crown restorations) fail to restore the natural biomineralized structure and often result in long-term complications, including polymerization shrinkage and marginal microleakage.[3,4] Hence, there is a pressing need in dental materials research to develop non-invasive remineralization techniques that can genuinely achieve "regeneration" of dental hard tissues.[5]

The essence of regeneration is biomimetic mineralization-a process that replicates the natural, orderly deposition of apatite regulated by an organic matrix. Compared to crystalline hydroxyapatite (HA), amorphous calcium phosphate (ACP) exhibits higher solubility and ionic activity, allowing it to infiltrate more effectively into the nanoscopic pores of demineralized tissue.[6,7] As a key kinetic precursor, ACP can guide the orderly deposition of minerals within collagen fibrils, making it an ideal foundation for achieving high-quality biomimetic mineralization.[8] However, pure ACP is highly unstable in solution and transforms rapidly into highly crystalline HA in a disordered manner. The resulting random crystals are unable to penetrate deeply into the nanoscopic pores of demineralized

---

[a] *Research Institute of Tissue Engineering and Stem Cells, Department of Stomatology, The Second Clinical College of North Sichuan Medical College, Nanchong, Sichuan 637000, China. E-mail: zhangchengdong@nsmc.edu.cn*

[b] *Collaboration Innovation Center for Tissue Repair Material Engineering Technology, China West Normal University, Nanchong, Sichuan 637002, China*

lesions and dentinal tubules.[9] This limitation substantially hinders the clinical effectiveness of ACP-based materials.

To address the stability of ACP, small organic molecules (SOM) have been used as potential modulators due to their ability to effectively regulate the crystallinity and morphology of calcium phosphate (CaP).[10] Compared to traditional resin-based materials, ACP-based nanomaterials exhibit enhanced biomimetic affinity and ion-releasing capabilities, making them highly effective for dentinal tubule occlusion.[11,12] These modulators, particularly with high negative charge density and low molecular weight, have been demonstrated to stabilize ACP nanoclusters and promote their penetration into the collagenous matrix. This mechanism, which aligns with the groundbreaking work by Zheng *et al.* demonstrating that specific charged SOM can directly mediate intrafibrillar mineralization through electrostatic matching,[13] is further exemplified in other effective systems, such as the gelatin-stabilized ACP coating developed by Feng *et al.*[14]

Indeed, the charged functional groups of organic molecules are central to their regulatory function. Negatively charged groups, such as carboxylate (COO^-) and phosphate (PO_4^{3-}), can bind to calcium ions (Ca^{2+}) through electrostatic attraction.[15–17] This interaction not only inhibits the excessive aggregation and disordered transformation of ACP precursors but also directs their orderly nucleation and growth on organic matrices such as collagen fibrils.[18] Recent studies have further demonstrated that polymers containing different negatively charged groups (*e.g.*, polyacrylic acid) can effectively stabilize ACP and enhance its remineralization and antibacterial properties.[19–21] However, a systematic comparative analysis of how the specific properties of different functional groups influence their interaction mechanisms with ACP, the microstructure of the resulting mineralized products, and their ultimate reparative efficacy is still lacking. Meanwhile, in dentistry, although ACP-based nanomaterials exhibit greater potential than traditional resin materials for sealing dentinal tubules,[22] the long-term stability and precise intra-tubular orientation of the formed minerals remain significant challenges.[23,24]

To investigate the effects of SOM with different chemical groups on CaP formation and dentin remineralization, this study employed phytic acid (IP6) and cyclohexanehexacarboxylic acid (H6L) as morphology modulators in CaP synthesis. The selection of these two molecules is strategically based on their structural symmetry yet distinct chemical functionalities, providing a controlled model to compare the influence of phosphate *versus* carboxyl groups. Both molecules possess a symmetric cyclohexanehexasubstituted backbone, but differ fundamentally in the chemical nature of their functional groups, as illustrated in Fig. 1. IP6, a naturally occurring organic phosphate ester in plants, carries six fully deprotonated PO_4^{3-} at physiological pH, conferring high negative charge and strong Ca^{2+}-chelating ability. In contrast, H6L contains six carboxyl groups, with a deprotonation degree that is pH-dependent.[25] The highly electronegative phosphate groups can effectively attract free Ca^{2+} in solution, facilitating the formation of necessary intermediates for precipitation and thus promoting CaP deposition.[26] Meanwhile, carboxyl-containing organic molecules, such as γ-carboxyglutamic acid in osteocalcin, have been shown to stabilize and promote the growth of nanoscale CaP ion clusters through direct interaction.[27] These studies indicate that both phosphate and carboxyl groups can enhance CaP formation and growth *via* distinct molecular pathways, and composites incorporating these functional groups generally demonstrate favorable cytocompatibility.[28,29]

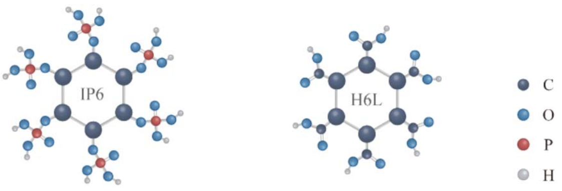

Fig. 1 The molecular structure of H6L and IP6.

Beyond their roles as crystal modulators, both molecules exhibit significant potential in tissue regeneration. Recent studies have further revealed that IP6 possesses intrinsic osteogenic bioactivity; for instance, it has been shown to improve the osteogenesis of bone marrow mesenchymal stem cells (BMSCs) by activating the ERK signaling pathway and exhibits potent antioxidant properties that support a pro-regenerative microenvironment.[30,31] Meanwhile, Xiao *et al.* successfully prepared CaP materials with different microstructures using H6L as a morphology regulator. *In vitro* cell assays demonstrated that when co-cultured with BMSCs, these materials exhibited good biocompatibility.[32] Therefore, the integration of IP6 and H6L not only regulates material synthesis but also aims to synergistically enhance the biological performance of the resulting composites for tissue repair.

This study aims to combine IP6 and H6L with ACP nanoclusters, respectively, to fabricate two nanocomposite materials: H6L/CaP and IP6/CaP. Through systematic physicochemical characterization and *in vitro* mineralization assays, their effects on dentin remineralization and repair will be comparatively analyzed at the micro- and nanoscale.

Materials and methods

Preparation and characterization of materials

In this study, SOM/CaP nanocomposites were prepared *via* a chemical co-precipitation method. The concentrations of calcium ions and phosphate ions in the reaction system were 10 mM and 6 mM, respectively, corresponding to a Ca/P molar ratio of 1.67, and the concentration of each SOM was 2 mM. The specific procedure was as follows: 0.026 mL of a 70% (w/w) aqueous solution of IP6 (Sinopharm Chemical Reagent, China) and 58.80 mg of calcium chloride dihydrate ($CaCl_2\cdot 2H_2O$, Sinopharm Chemical Reagent, China) were first dissolved together in 20 mL of deionized water. Subsequently, 20 mL of an aqueous solution containing 41.76 mg of dipotassium hydrogen phosphate (K_2HPO_4, Sinopharm Chemical Reagent, China) was added dropwise to the above mixture, and the pH of the above solution was adjusted at 7.0 using a KOH (Sinopharm Chemical Reagent, China) solution. After the reaction, the precipitate was collected by filtration, thoroughly washed sequentially with deionized water and ethanol, collected by centrifugation and freeze-dried to obtain the IP6/CaP product. The H6L/CaP product was prepared following the same procedure, except that the IP6 aqueous solution was replaced with 13.5 mg of H6L powder (Sinopharm Chemical Reagent, China). The control sample, prepared without the addition of any organic molecules, was designated as CaP. 45S5 bioactive glass (BG, particle size ≤20 μm) composed of 45 wt% SiO_2, 24.5 wt% CaO, 24.5 wt% Na_2O, and 6 wt% P_2O_5, was obtained from Hebei Yougu Biotechnology Co., Ltd, China.

To observe the morphology of the samples, CaP, IP6/CaP, and H6L/CaP were separately dispersed in anhydrous ethanol (purity ≥ 99.5%), ultrasonicated for 5 minutes, and then dropped onto carbon-coated copper grids. The morphology and structure were analyzed using transmission electron microscopy (TEM, Tecnai G2 F30, FEI, Holland) and selected area electron diffraction (SAED). Phase composition analysis of the samples was performed using an X-ray diffractometer (D8 ADVANCE, Bruker AXS, Germany) under the following scanning conditions: 2θ range of 10°–60°, step size of 0.02°, and scanning speed of 2° min^{-1}. Fourier transform infrared (FTIR) spectra were obtained using an FTIR spectrometer (Vertex 70, Bruker, Germany) in attenuated total reflection (ATR) mode. For dynamic light scattering (DLS) and zeta potential measurements, each dried powder was added to anhydrous ethanol at a concentration of 0.5 mg mL^{-1}, and the zeta potential was measured using a laser particle size analyzer (Malvern Instruments, UK) at a voltage of 50 V and a temperature of 25 °C.

Self-mineralization performance of materials

After being compressed into pellets (0.01 g each), CaP, IP6/CaP and H6L/CaP powders were immersed separately in 5 mL of artificial saliva solution and incubated statically in a 37 °C water bath for 12 h and 7 days. The artificial saliva was prepared in compliance with ISO 10271 standards (0.400 g per L NaCl, 0.400 g per L KCl, 0.795 g per L $CaCl_2\cdot 2H_2O$, 0.690 g per L $NaH_2PO_4\cdot 2H_2O$, 0.005 g per L $Na_2S\cdot 9H_2O$, and 1.000 g per L CH_4N_2O).[33] The mineralization morphology and composition on the surface of each sample were subsequently examined and evaluated using scanning electron microscopy (SEM, Sigma360, Germany) and FTIR.

Preparation of collagen electrospun membranes

Type I collagen (BS929, Biosharp, China) and polycaprolactone (PCL, Aladdin, China) were co-dissolved in 5 mL of hexafluoroisopropanol at amounts of 0.67 g and 0.33 g, respectively, to prepare an electrospinning solution with a total concentration of 20% (w/v). The solution was loaded into a 5 mL syringe equipped with a metal needle having an inner diameter of 0.21 mm. Electrospinning was performed at room temperature under the following parameters: an applied voltage of approximately +10 kV, a needle-to-collector distance of 10 cm, a voltage of −2 kV applied to the collector, a solution feed rate of 1.0 mL h^{-1}, and a spinning duration of 4 h. The resulting fibrous membrane was placed in a vacuum drying oven and dried at room temperature under a vacuum of 1 torr for 24 h to obtain the final dried electrospun collagen membrane.

Biomimetic mineralization of electrospun collagen membranes

Collagen electrospun membranes were secured at the bottom of 6-well plates. To each well, 2 mL of artificial saliva containing carboxymethyl cellulose (CMC, Goldbio, Beijing, China) and 2 mM suspensions of IP6/CaP, H6L/CaP, or CaP alone were added, designated as C + IP6/CaP, C + H6L/CaP, and C + CaP, respectively. A pure collagen electrospun membrane without any additive was used as the control (C). After incubation for 3 and 7 days, the liquid in each well was aspirated, and the membranes were gently rinsed three times with deionized water. Following removal of residual liquid, the surface mineralization morphology of the samples was examined by SEM.

Preparation of dentin demineralization model

All experiments were performed in accordance with the Declaration of Helsinki and the national ethical guidelines for biomedical research involving human subjects (No. 4 [2023] of the National Health Commission of China). The study was approved by the Medical Ethics Committee of Nanchong Central Hospital (Approval No. 2025-YS-205). All human extracted teeth used in this study were obtained from discarded teeth extracted during clinical treatments for reasons such as orthodontics or periodontal disease. Informed consents were obtained from human participants of this study. Freshly extracted, caries-free human third molars with intact crowns were collected and stored in physiological saline at 4 °C for use within one month. The teeth were sectioned coronally using a diamond saw attached to a micro-motor to obtain dentin discs approximately 1 mm thick. The dentin surfaces were then sequentially ground under running water with 800, 1500, 2000, and 3000 grit silicon carbide paper until a smooth, flat surface was achieved. Finally, the specimens were immersed in a 35% phosphoric acid solution for 30 s to expose the dentin tubules.

Preparation of toothpaste

A commercially available toothpaste containing 0.1% fluoride (Darlie toothpaste, China) was used as the control group, designated as F. The experimental toothpastes were prepared by uniformly blending CaP, IP6/CaP, H6L/CaP, or BG powder (each at 5 wt%) into the fluoride-containing Darlie toothpaste. The resulting formulations were labeled as F + CaP, F + IP6/CaP, F + H6L/CaP, and F + BG, respectively. To ensure the uniform dispersion of nanoparticles within the viscous matrix, a dual-syringe homogenization technique was employed. Specifically, the respective powders and the base toothpaste were loaded into two separate 5 mL syringes, which were then coupled using a short, tightly-fitted plastic tube. The mixture was homogenized through 50 cycles of manual inter-syringe extrusion, achieve a visually uniform, air-free paste. All prepared samples were sealed in light-shielded aluminum tubes and stored at 4 °C.

Evaluation of dentin surface adhesion of calcein-labeled materials

Calcein-labeled suspensions of BG, CaP, IP6/CaP, and H6L/CaP were prepared. The labeling procedure was as follows: 0.2 g of each powder (CaP, IP6/CaP, H6L/CaP, or BG) was mixed with 1 mL of a 100 μg per mL calcein solution. After incubation in the dark for 30 min, the labeled particles were collected through repeated washing and centrifugation, followed by drying at 60 °C for 12 h. Fluorescence micrographs of the dentin surfaces were taken after a single treatment with the calcein-labeled toothpaste and subsequent immersion in artificial saliva for 12 h to visualize the distribution of BG, CaP, IP6/CaP, and H6L/CaP particles.

Evaluation of dentin tubule occlusion *in vitro*

Acid-etched dentin specimens with exposed tubules were randomly allocated to four groups and subjected to twice-daily brushing (morning and evening) using one of the four prepared toothpastes. Simulated brushing was performed by applying a pea-sized amount of toothpaste to the head of an electric toothbrush, which was operated at 150 rpm under a 175 g load for 60 s per specimen. After each brushing cycle, specimens were rinsed with deionized water to remove residual toothpaste and subsequently immersed in artificial saliva at 37 °C until the next brushing session. Following 7 days of treatment, the dentin specimens were rinsed three times with deionized water, dried overnight at 60 °C, and examined using SEM. For each specimen, at least three images were captured from different random locations under SEM. The percentage of exposed dentin tubule area in SEM images was calculated using Image J software as the following formula:

$$\begin{aligned}&\text{Exposed dentin tubule area (\%)}\\&=(\text{exposed dentin tubule area/total area})\times 100\%\end{aligned}$$

Acid resistance stability

To evaluate the acid resistance stability of occluded dentin tubules, dentin specimens treated with the F + BG, F + CaP, F + IP6/CaP and F + H6L/CaP toothpastes were immersed in a 6% citric acid solution for 1 min. After acid challenge, the specimens were rinsed three times with deionized water and then examined by scanning electron microscopy (SEM). Furthermore, the percentage of exposed dentin tubule area was calculated according to the formula described in the previous section.

Cytotoxicity assay of extracts from IP6/CaP, H6L/CaP, CaP, and BG

The powders of BG, CaP, IP6/CaP and H6L/CaP were sterilized by UV irradiation for 6 h. Subsequently, 10 mg of each sterilized powder was placed into a 15 mL centrifuge tube containing 10 mL of complete DMEM/F12 medium and incubated in a cell culture incubator for 72 h to prepare the extracts. After centrifugation, the supernatant was collected as a 1000 μg per mL stock extract solution, which was then diluted to concentrations of 500 μg mL^{-1} and 100 μg mL^{-1} for subsequent use.

Human skin fibroblasts (HSF) were digested, centrifuged, counted, and diluted to a concentration of 8 × 10^3 cells per mL. The cell suspension was seeded into 96-well plates at 100 μL per well. After 24 h of attachment, the culture medium was replaced with the corresponding extract solutions. The extracts were refreshed every 48 h. At 24 h, 48 h, and 72 h, 110 μL of CCK-8 reagent was added to each well and incubated in the dark for 1 h. Then, 100 μL of the CCK-8 solution from each well was transferred to a new plate, and the absorbance was measured at 450 nm using a microplate reader. High-density polyethylene and 0.64% phenol in medium were used as the negative and positive controls, respectively.

The biocompatibility of the materials was graded according to the National Standard (GB/T 16886.5-2017) based on the relative growth rate (RGR) of cells: RGR > 100% (Grade 0); RGR > 80% (Grade 1); RGR > 50% (Grade 2); RGR > 30% (Grade 3); RGR > 0% (Grade 4). The same procedure was performed to evaluate biocompatibility at extract concentrations of 500 μg mL^{-1} and 1000 μg mL^{-1}. Additionally, cell viability was visualized using a Calcein-AM/PI double-staining kit (Invitrogen, USA).

Statistical analysis

All quantitative data were expressed as the mean ± standard deviation (SD). Statistical analysis was performed using GraphPad Prism 9.5.0 software. Comparisons among multiple groups were conducted using one-way analysis of variance (ANOVA). A *P*-value < 0.05 was considered statistically significant.

Results

Characterization of CaP, IP6/CaP and H6L/CaP

The preparation process of IP6/CaP and H6L/CaP was illustrated in Fig. 2A. SEM results (Fig. 2B) revealed significant morphological differences among the CaP, IP6/CaP, and H6L/CaP samples. Combined with the low-magnification TEM images (Fig. 2C, upper right corners), the CaP group exhibited a typical thin plate-like morphology, whereas both the IP6/CaP and H6L/CaP groups formed relatively uniform spherical nanoparticles. High-resolution TEM images (Fig. 2C) showed clear lattice fringes in the CaP group, and the corresponding SAED patterns (Fig. 2C, lower right corners) displayed partially resolved polycrystalline diffraction rings, indicating a poorly crystalline CaP phase. In contrast, no obvious lattice fringes were observed in the high-resolution images of the IP6/CaP and H6L/CaP groups, and their SAED patterns exhibited only diffuse halo rings, confirming that both were predominantly amorphous structures. This transition in morphology and crystallinity can likely be attributed to the interference of the introduced SOM with the nucleation and growth processes of CaP crystals. EDS mapping (Fig. 2D) confirmed the presence of calcium, phosphorus, oxygen, and carbon in all three groups. Notably, the carbon content in the IP6/CaP and H6L/CaP samples was significantly higher than that in the CaP group, verifying the successful incorporation of the SOM and their role in modulating the crystallization process, thereby altering the morphology and structure of the materials.

Based on the XRD patterns (Fig. 3A), distinct differences in crystallinity were observed among the three groups. The CaP

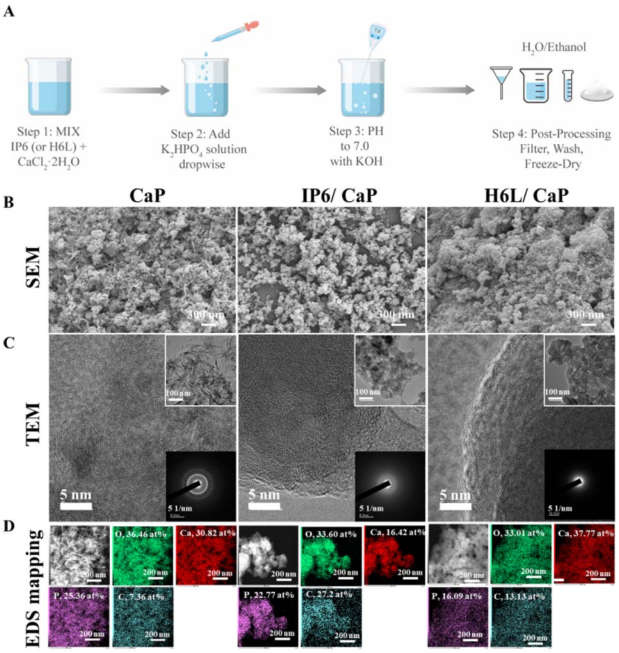

Fig. 2 (A) Schematic diagram of IP6/CaP and H6L/CaP preparation process; (B) SEM images of CaP, IP6/CaP, and H6L/CaP; (C) TEM images of CaP, IP6/CaP, and H6L/CaP at low (upper right insets) and high magnifications, with the corresponding SAED patterns inset at the bottom-right corner; (D) corresponding EDS elemental mappings.

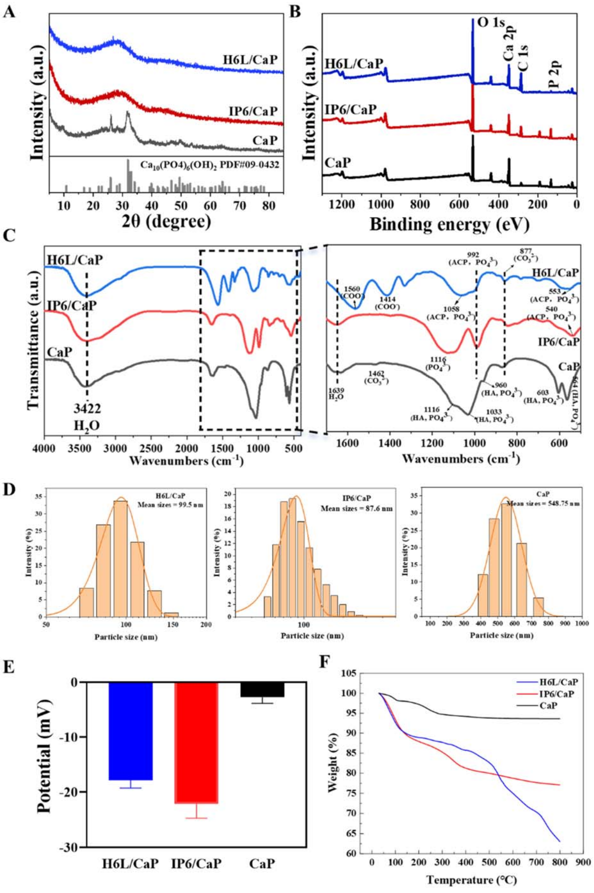

Fig. 3 Physicochemical characterization of the samples. (A) XRD, (B) XPS, (C) FTIR, (D) hydrodynamic size, (E) zeta potential, (F) TGA.

sample exhibited weak peaks at 25.8° and 32.2°, corresponding to the (002) and (112) lattice planes of HA (JCPDS 09-0432), respectively, indicating its poor crystallinity. In contrast, both IP6/CaP and H6L/CaP samples showed only a broad hump in the 20°–35° range, characteristic of ACP, which is consistent with the TEM results and indicates that the introduced organic ligands (IP6 and H6L) effectively inhibited the crystallization of CaP, transforming it from crystalline HA into amorphous phosphate. XPS survey spectra (Fig. 3B) indicated that all samples exhibited characteristic peaks for Ca 2p, P 2p, O 1s, and C 1s. Compared with pure CaP, the H6L/CaP and IP6/CaP groups showed significantly enhanced C 1s signals, which was consistent with the EDS mapping results and further confirmed the successful integration of the organic molecules with CaP.

The FTIR spectra of all products (Fig. 3C) displayed a broad absorption band at 3422 cm^{-1} and a narrow bending vibration peak near 1639 cm^{-1}, which are attributed to adsorbed water molecules typically retained on the powder surface during synthesis.[34] The CaP group exhibited characteristic HA peaks. Specifically, the bands at 564 cm^{-1} and 603 cm^{-1} were attributed to the bending vibrations of PO_4^{3-}, while the bands at 960 cm^{-1}, 1033 cm^{-1}, and approximately 1116 cm^{-1} corresponded to the stretching vibrations of PO_4^{3-}. Additionally, weak peaks observed at 877 cm^{-1} and 1462 cm^{-1} were attributed to the substitution of CO_3^{2-} for PO_4^{3-}, indicating the formation of B-type carbonated hydroxyapatite, which is commonly observed in biological apatites.[34,35] For the IP6/CaP group, a broad peak was observed at 1116 cm^{-1}, which is attributed to the overlapping absorption of PO_4^{3-} from phytic acid and ACP.[36–38] The band located at 992 cm^{-1} corresponds to the characteristic absorption peak of ACP, while the absorption band observed near 540 cm^{-1} is assigned to the ν_4 bending vibration mode of PO_4^{3-} in ACP.[37] In the H6L/CaP group, the FTIR spectrum exhibited characteristic absorption peaks attributed to COO^- at 1560 cm^{-1} and 1414 cm^{-1}.[35] In the phosphate vibration region, the broad peak at 1058 cm^{-1} was assigned to the vibration of PO_4^{3-} in ACP, while the band at 992 cm^{-1} corresponded to the characteristic absorption peak of ACP.[37] Additionally, the absorption band observed near 553 cm^{-1} was attributed to the ν_4 bending vibration mode of PO_4^{3-} in ACP.[35,37] Collectively, these results confirm that IP6 and H6L were successfully incorporated into CaP.

DLS measurements (Fig. 3D) showed that the average hydrodynamic diameters of IP6/CaP and H6L/CaP were 87.64 ± 2.37 nm and 99.56 ± 1.67 nm, respectively, substantially smaller than that of pure CaP (548.75 ± 2.32 nm), indicating effective size regulation by the organic modifiers. Moreover, the surface negativity of the composites increased markedly, with zeta potentials (Fig. 3E) of −22.2 mV for IP6/CaP and −17.8 mV for H6L/CaP, compared to −2.77 mV for pure CaP. This enhanced negative charge favors the electrostatic attraction and enrichment of positively charged mineral precursors (*e.g.*, Ca^{2+}) in solution, thereby promoting heterogeneous nucleation on target surfaces such as collagen fibers and providing a basis for the remineralization capability of the materials.[39–41]

TGA results (Fig. 3F) showed that CaP exhibited the first stage of weight loss between 30–130 °C, primarily attributed to the removal of adsorbed water, with a content of approximately 1.9%. The second stage of weight loss occurred between 130–380 °C, mainly corresponding to the removal of crystalline water, with a content of approximately 3.8%, after which the sample mass stabilized. For IP6/CaP, the weight loss between 30–230 °C corresponded to the removal of adsorbed and crystalline water, with a total water content of approximately 12.4%. The decomposition of the IP6 occurred between 230–480 °C, with a content of approximately 7.1%, after which the sample stabilized. For H6L/CaP, the weight loss between 30–400 °C was attributed to adsorbed and crystalline water, with a content of approximately 14.1%. The decomposition of the H6L occurred between 220–680 °C, with a content of approximately 14.8%. These results indicated that the successful incorporation of IP6 and H6L significantly influenced the hydration behavior and thermal decomposition characteristics of CaP.

Self-mineralization ability of CaP, IP6/CaP, and H6L/CaP

To evaluate the inherent bioactivity and chemical stability of the materials, CaP, IP6/CaP, and H6L/CaP were compressed into disk-shaped samples and immersed in artificial saliva for 12 h and 7 days. After immersion, the surface mineralization morphology was observed by SEM, and the functional group composition of the surface mineralization products was analyzed by FTIR.

SEM results (Fig. 4A) showed that after 12 h of immersion, all three groups presented relatively dense surfaces. Corresponding FTIR spectra (Fig. 4B) showed no significant changes compared to those before mineralization (Fig. 3C), indicating that the material surfaces were likely in an early nucleation stage of mineralization induction, without obvious crystal formation. The CaP group exhibited characteristic HA peaks (1116, 1033, 960, 603, 564 cm^{-1}). Both the IP6/CaP and H6L/CaP groups displayed typical ACP absorption features, including a characteristic peak at 992 cm^{-1} and the ν_4 bending vibration of PO_4^{3-} around 540–560 cm^{-1}. In addition, the IP6/CaP group showed a broad peak at 1116 cm^{-1}, attributed to the overlap of PO_4^{3-} absorption from phytic acid and ACP, while the H6L/CaP group retained the characteristic COO^- peaks (1560 and 1414 cm^{-1}). After 7 days of immersion, distinct differences in surface morphology were observed among the groups. The CaP group exhibited disordered sheet- and needle-like structures with evident cracks and bulky aggregates, which may result from random heterogeneous nucleation and crystal overgrowth in artificial saliva. In contrast, the organically modified IP6/CaP and H6L/CaP groups displayed regular surface morphologies, consisting of densely packed, uniformly sized round-shaped nanoparticles with clear boundaries and overall smooth surfaces, reflecting a more ordered and controllable mineralization process. FTIR analysis further confirmed the changes in the chemical composition of the mineralization products. After 7 days of mineralization, the characteristic absorption peaks originally attributed to IP6 and H6L in the IP6/CaP and H6L/CaP samples disappeared, and the characteristic peaks of ACP also vanished. All three groups exhibited characteristic PO_4^{3-} absorption bands around 1089, 983, and 560 cm^{-1}. This indicates that after 7 days of mineralization, the ACP in both the IP6/CaP and H6L/CaP groups had transformed into HA. The organic molecules primarily functioned as regulators during the ordered mineralization process and were not retained in the final mineral phase.

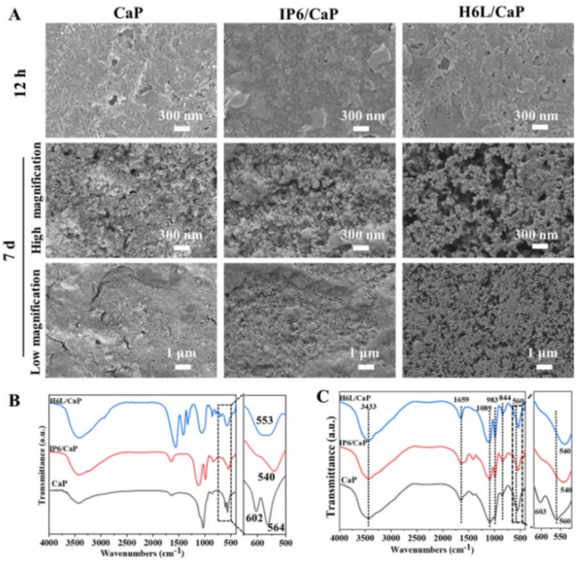

Fig. 4 Self-mineralization performance evaluation of CaP, IP6/CaP, and H6L/CaP immersed in artificial saliva for 12 h and 7 days. (A) SEM; (B) FTIR spectra after 12 h of immersion; (C) FTIR spectra after 7 days of immersion.

Mineralization capacity of CaP, IP6/CaP, and H6L/CaP on type I collagen

To further evaluate the mineralization capacity of the materials, collagen electrospun membranes were first fabricated. These membranes were then immersed in artificial saliva containing the respective materials for mineralization periods of 3 and 7 days, followed by SEM observation of their surface mineralization morphology. As shown in Fig. 5A, the as-prepared collagen membrane consisted of interwoven fibers with diameters of approximately 400–600 nm, exhibiting a straight morphology. After 3 days of mineralization (Fig. 5B), fibers in all groups appeared curved and showed signs of degradation. The C group displayed no obvious mineral formation. The C + CaP group exhibited unevenly distributed mineral deposits, the C + IP6/CaP group showed round-shaped particle deposition, and the C + H6L/CaP group formed microscale petal-like particles. After 7 days, degradation in group C further intensified, still without significant mineral deposition. EDS mapping detected only sparse distribution of Ca and P elements on its surface, indicating a low degree of mineralization. In contrast, the other three groups all exhibited considerable mineral deposition, with EDS mapping confirming abundant Ca and P signals.

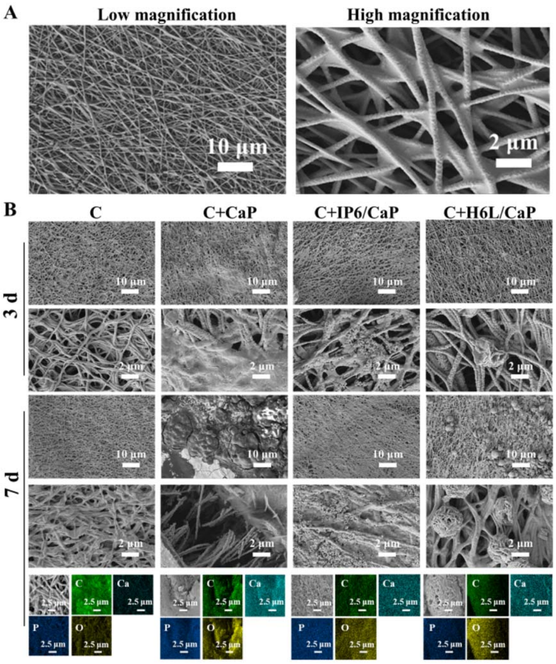

Fig. 5 (A) SEM images of the electrospun collagen membranes; (B) SEM images and EDS mapping of the C, C + CaP, C + IP6/CaP, and C + H6L/CaP after mineralization for 3 and 7 days.

Specifically, the C + CaP surface was completely covered by large, irregular mineral aggregates that filled the fiber interstices. This mineral layer was highly non-uniform, exhibited cracks, and appeared detached from the fibers, making it prone to washing off. The C + IP6/CaP group formed a uniform and continuous mineral coating on the fiber surfaces, where nanoparticles completely covered the collagen fibers, resulting in a blurred interface and a fused state between the mineral and the fiber. In the C + H6L/CaP group, the microscale petal-like particles on the fiber surfaces increased further, with a relatively uneven distribution; some fibers were completely covered, In summary, the mineralization capacity of the different groups can be ranked as C + IP6/CaP > C + H6L/CaP > C + CaP. The C + IP6/CaP group achieved the most effective and stable biomimetic mineralization, forming a dense and uniform coating that integrated seamlessly with the collagen fibers. While the C + H6L/CaP group also promoted mineralization, its distribution was less consistent. The C + CaP group showed the weakest performance, with minerals forming irregular clusters that lacked strong adhesion to the membrane surface.

Dentin slice preparation and evaluation of toothpaste adhesion on dentin

Human third molars were collected and sectioned into slices measuring 5 × 5 × 1 mm^3, following the procedure illustrated in Fig. 6. After acid-etching, the dentin surface revealed clearly exposed dentinal tubules. Prior to evaluating the effectiveness of each material in occluding dentinal tubules, their adhesion to the dentin surface was examined. First, all material groups were fluorescently labeled with calcein. As shown in Fig. 7A, the calcein-labeled materials and their corresponding toothpaste mixtures exhibited green fluorescence. After a single treatment of dentin with the labeled toothpaste (Fig. 7B), more green fluorescent particles were observed on the dentin surface in the F + CaP@C, F + H6L/CaP@C, and especially the F + IP6/CaP@C groups compared to the F + BG@C group.

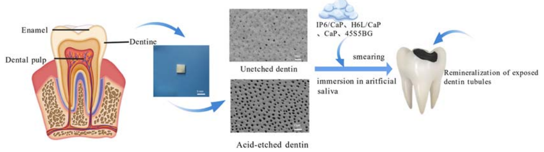

Fig. 6 Flowchart of tooth slice preparation and subsequent experiments.

Quantitative analysis (Fig. 7D) revealed that the percentage of fluorescent area followed the order: F + IP6/CaP@C > F + H6L/CaP@C > F + CaP@C > F + BG@C. Subsequently, the treated dentin samples were immersed in artificial saliva for 12 h to reassess particle retention (Fig. 7C). Although both the fluorescence area and intensity decreased noticeably in the F + IP6/CaP@C and F + H6L/CaP@C groups, distinct green particles remained on the dentin surface. In contrast, almost no fluorescent particles were detected in the F + BG@C and F + CaP@C groups. Quantitative results (Fig. 7E) confirmed that the

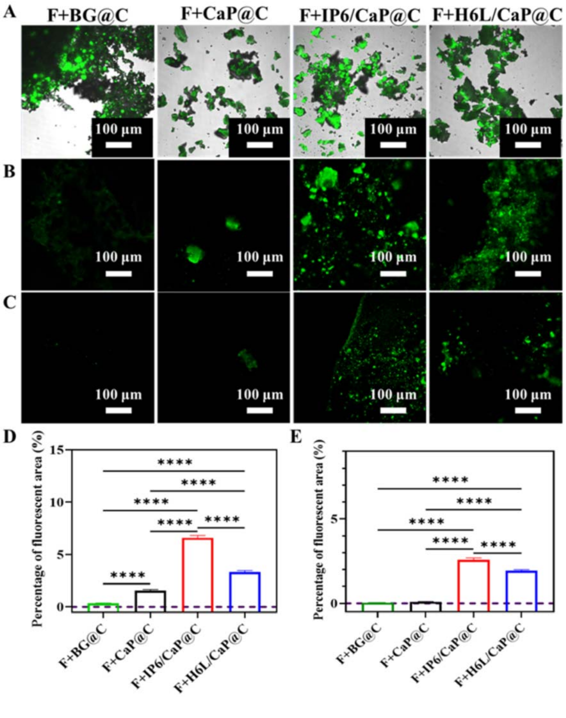

Fig. 7 Evaluation of dentin surface adhesion of toothpastes containing calcein-labeled samples. (A) Fluorescence microscopy images of toothpastes incorporated with calcein-labeled materials. Fluorescence microscopy images of dentin surfaces after a single treatment with calcein-labeled toothpaste (B) and after subsequent immersion in artificial saliva for 12 h (C). Area percentage of the residual fluorescent region after a single treatment (D) and after 12 h of immersion in artificial saliva (E).

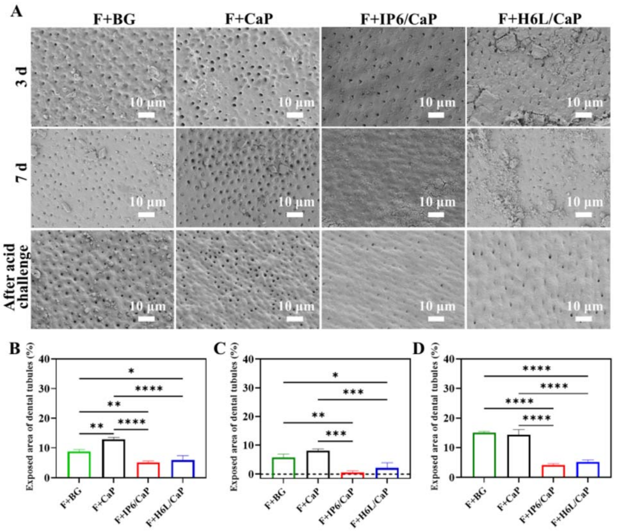

Fig. 8 Evaluation of dentinal tubule occlusion efficacy and acid resistance stability by different toothpastes. (A) Representative SEM images of dentin surfaces after 3 days and 7 days of treatment in an *in vitro* brushing model, and subsequent citric acid challenge. (B–D) Statistical analysis of the percentage of exposed dentinal tubule area after 3 days toothpaste treatment (B), 7 days toothpaste treatment (C), and post-citric acid treatment (D). $^{*}p < 0.05$, $^{**}p < 0.01$, $^{***}p < 0.001$, $^{****}p < 0.0001$.

fluorescent area percentage was highest for F + IP6/CaP@C, followed by F + H6L/CaP@C, while the F + BG@C and F + CaP@C groups showed the lowest values.

Occlusion of dentinal tubules and acid resistance evaluation of toothpaste

To simulate daily brushing habits, dentin samples were treated *in vitro* with toothpaste containing BG, CaP, IP6/CaP, or H6L/CaP particles, and the dentinal tubule occlusion effect was evaluated by SEM, as shown in Fig. 8A. After 3 days of treatment, all groups exhibited varying degrees of tubule occlusion. The F + CaP group showed almost no effective mineral deposition on the dentin surface, while the F + H6L/CaP group displayed relatively uneven mineral deposits that covered most tubule openings. Quantitative results (Fig. 8B) indicated that the exposed tubule area followed the order: F + CaP > F + BG > F + H6L/CaP > F + IP6/CaP. After 7 days, the F + IP6/CaP group achieved a substantially dense and uniform occlusion layer over the tubules. The occlusion effect in the F + H6L/CaP group also improved, though the deposits appeared loosely bound to the substrate; nevertheless, most tubule openings were nearly completely sealed. The F + CaP and F + BG groups showed slight improvement compared to 3 days, but scattered, irregular large crystals were visible on the surface, and the dentinal tubule openings remained largely exposed. Statistical results (Fig. 8C) confirmed that the exposed tubule areas in the F + IP6/CaP and F + H6L/CaP groups were significantly lower than those in the F + CaP and F + BG groups.

After acid treatment, the exposed tubule area increased in all groups (Fig. 8D), but the values for the F + IP6/CaP and F + H6L/CaP groups remained markedly lower than those of the F + CaP and F + BG groups. This demonstrates the effective tubule occlusion and acid-resistant stability of the F + IP6/CaP and F + H6L/CaP groups *in vitro*. The strong adhesion of IP6 and H6L particles to the dentin surface, along with their good stability in artificial saliva, promoted the accumulation and penetration of these particles into dentinal tubules. In contrast, CaP and BG particles exhibited poor adhesion to dentin, making them susceptible to being washed away under mechanical brushing forces and acid attack, leading to re-exposure of the tubules.

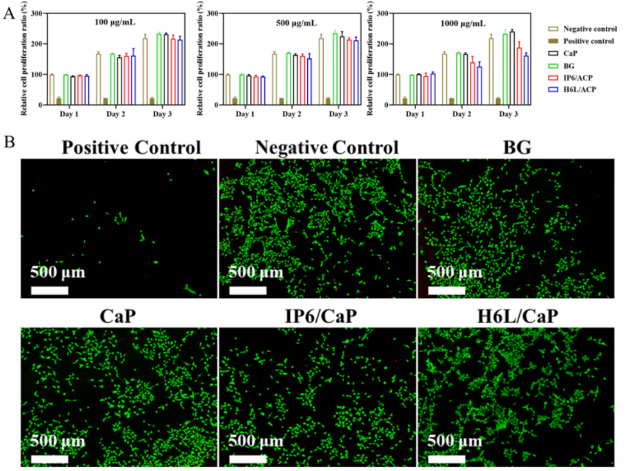

Fig. 9 Evaluation of the cytocompatibility of the materials. (A) Cell viability was measured by the CCK-8 assay after culture in material extracts at various concentrations for different time periods. (B) Representative fluorescence images of live/dead staining for cells cultured in 100 μg per mL extract for 1 day.

Cell compatibility

The cytotoxicity of BG, CaP, IP6/CaP, and H6L/CaP toward HSF cells was evaluated using CCK-8 assay and live/dead staining. As shown in Fig. 9A, no significant cytotoxic effects were observed for any material group under different extract concentrations and incubation periods. Compared with the negative control, the relative proliferation rates of HSF cells cultured with material extracts on days 1, 2, and 3 all remained above 80%. According to the National Standard GB/T 16886.5-2017, this result falls within the grade 0–1 biocompatibility range, indicating favorable cytocompatibility for all tested materials.

To further verify biocompatibility, live/dead staining was performed. After incubation with 100 μg per mL extracts (Fig. 9B), HSF cells in all groups exhibited high-density green fluorescence (live cells) with minimal red fluorescence (dead cells), consistent with the CCK-8 results. This confirms that at the tested concentrations, none of the four material extracts induced obvious cytotoxicity, further supporting their good biocompatibility.

Discussion

To develop ACP-based nanomaterials for caries repair and dentin hypersensitivity treatment, this study utilized two structurally similar SOM, IP6 and H6L, which differ in their chemical functional groups, as regulators. Using a simple chemical precipitation method, IP6/CaP and H6L/CaP nanoparticles with a size of approximately 100 nm were synthesized at room temperature. In the absence of organic regulators, the synthesized CaP was primarily HA. In contrast, when IP6 or H6L was added, the resulting CaP was predominantly ACP. Subsequently, the performance of these materials in dentin remineralization, dentin tubule occlusion, and acid resistance was systematically compared. The results showed that IP6/CaP exhibited the most effective promotion of dentin tubule occlusion and formation of a uniform and stable mineralized layer, followed by H6L/CaP. Both formulations outperformed pure CaP and commercial BG.

Traditional dentin remineralization therapies, such as those involving fluoride and bioactive glass, often focused on enhancing the acid resistance of the tooth surface or providing calcium and phosphate ions to create a localized supersaturated microenvironment for rapid mineralization.[42–44] Although these methods achieved notable success in caries prevention, their mode of action primarily relied on surface mineral accumulation, which often failed to achieve deep occlusion of dentinal tubules and ordered intrafibrillar mineralization of collagen.[45,46] Therefore, transitioning from "surface mineral accumulation" to "biomimetic structural repair" emerged as a key research focus in the field of dental materials. In recent years, CaP, as the primary inorganic constituent of dentin, garnered significant attention in dentin repair research due to its excellent biocompatibility and ion-releasing capability.[47] However, pure-phase CaP was highly unstable in physiological environments and prone to rapid disordered phase transformation, leading to the formation of large HA crystals that could hardly penetrate the nanoscale collagen pores of demineralized dentin. To address this bottleneck, researchers gradually turned their attention to ACP. As a natural precursor to HA formation, ACP possessed higher solubility and ionic activity, enabling effective penetration into the deep layers of demineralized tissue, and was thus regarded as an ideal "seed" for achieving intrafibrillar mineralization.[48,49] However, ACP was highly unstable and readily transformed into HA, posing a significant challenge for its practical application.

Currently, multiple strategies have been employed to stabilize ACP, such as utilizing carboxylate-rich polymers (*e.g.*, poly (acrylic acid)) to chelate calcium ions and inhibit the rapid phase transformation of ACP, or employing biomacromolecules (*e.g.*, casein phosphopeptides, gelatin) to stabilize ACP through steric hindrance and electrostatic interactions.[50,51] However, these approaches are often limited by proteolytic degradation, high cost, or suboptimal kinetic control. In contrast, SOM enriched with negatively charged groups (*e.g.*, IP6, H6L) offered the potential to overcome these limitations due to their high charge density and suitable molecular size. In this study, IP6 and H6L were selected to regulate the growth of CaP, leading to the successful synthesis of ACP nanoparticles. In the absence of SOM in the solution, the resulting CaP phase was HA. This indicated that both IP6 and H6L effectively stabilized ACP and inhibited its transformation into HA. This stabilization was likely attributed to the six phosphate groups of IP6, which exhibited a strong chelation affinity for Ca^{2+}, enabling rapid adsorption onto the surface of nascent CaP clusters, thereby reducing local supersaturation and sterically blocking crystal growth sites[52,53] Similarly, H6L, with its six symmetric carboxylate groups, functioned through an analogous dual mechanism involving chelation-mediated supersaturation reduction and surface adsorption-induced steric hindrance.[54] This synergistic action significantly elevated the activation energy barrier required for the dissolution–recrystallization pathway, thereby prolonging the stability of the amorphous precursor.[55] Compared to the un-stabilized control group, this stabilizing effect was particularly pronounced: in the absence of IP6 or H6L, CaP clusters rapidly and spontaneously rearranged into thermodynamically stable crystalline HA;[10,56,] whereas the presence of IP6 and H6L maintained their amorphous structure, preserved high reactivity, and resulted in the formation of smaller, more stable ACP nanoparticles with slower transformation kinetics.[57,58]

The binding affinity between the restorative material and the dentin surface was one of the critical factors affecting dentin repair. In the complex and dynamic oral environment, an ideal restorative material was not only required to possess pro-mineralization capability but also needed to firmly adhere to the dentin surface to withstand mechanical challenges such as toothbrushing, salivary flow, and masticatory stress, thereby providing a foundation for the sustained deposition of subsequent minerals. Typically, inactive ingredients or physically deposited particles in conventional toothpaste only loosely covered the tooth surface and were easily rinsed away during mouth rinsing or toothbrushing. In this study, ACP was incorporated into toothpaste to investigate its adhesion on the dentin surface. As a well-established material in clinical dentistry, BG functions as a commercial reference and a potent ionic reservoir, facilitating the continuous release of mineral precursors to drive the remineralization process.[59] Based on SEM images and quantitative analysis of calcein-labeled materials after toothpaste treatment (Fig. 7), the F + H6L/CaP@C and F + IP6/CaP@C groups exhibited significantly stronger binding to the dentin surface compared to the F + BG@C and F + CaP@C groups. This enhanced binding was likely attributable to the smaller nanoscale size of IP6/CaP and H6L/CaP, as well as the strong affinity of the abundant phosphate and carboxyl groups on the nanoparticle surfaces for calcium ions in dentin. In contrast, the F + BG@C and F + CaP@C groups, possibly due to the lack of effective chemical bonding, were more prone to detachment under mechanical challenges.

Furthermore, intrafibrillar mineralization, characterized by the infiltration of minerals into the collagen fibrils to form a hybrid structure analogous to natural dentin, was considered a hallmark of ideal dentin repair.[60] As shown in Fig. 5, the IP6/CaP treatment resulted in well-integrated mineral-fibril structures with seamless interfaces. Concurrently, the effective occlusion of dental tubules represented another crucial prerequisite for alleviating dentin hypersensitivity, preventing bacterial invasion, and ensuring the long-term stability of the restoration. As illustrated in Fig. 8, following treatment with

IP6/CaP and H6L/CaP nanocomposites, a continuous, uniform, and dense mineralized layer was formed on the demineralized dentin surface. The reparative efficacy of both groups was significantly superior to that of the pure CaP group and the bioactive glass group. This remarkable performance was likely attributed to a synergistic mechanism combining physical penetration and chemical remineralization.

According to previous reports, particle size and binding affinity were identified as the primary factors determining tubule occlusion efficiency.[61,62] The TEM (Fig. 2C) and DLS (Fig. 3D) results from this study confirmed that the IP6/CaP and H6L/CaP nanoparticles, stabilized by SOM, possessed particle sizes below 100 nm and exhibited excellent dispersibility, which facilitated their deep penetration into the tubules under mechanical brushing action. Once localized within the tubules, these amorphous nanoparticles, characterized by high solubility and ionic activity, functioned as sacrificial "ion reservoirs". Subsequently, the dissolution of these ACP clusters elevated the local concentrations of Ca^{2+} and PO_4^{3-} ions, creating a supersaturated microenvironment that drove the reprecipitation and growth of stable HA crystals onto the tubule walls and collagen matrix. This transition from initial "particle filling" to active "mineral growth" ensured the formation of a dense and acid-resistant occlusive layer. The particularly outstanding performance of the IP6/CaP group was likely associated with the stronger Ca^{2+} chelation capacity and steric hindrance effect conferred by its six phosphate groups, which more effectively prolonged the stability period of ACP and guaranteed the ordered growth of minerals.

Compared with previously reported biomimetic systems utilizing high molecular weight polymers (*e.g.*, polyacrylic acid, PAA), biomimetic peptides, or other biological macromolecules, the IP6/CaP system proposed in this study exhibited multiple advantages. Benefiting from their suitable size and biomimetic affinity, the IP6/CaP and H6L/CaP nanocomposites were able to readily penetrate into the nanopores and tubule interiors of demineralized dentin. Once internalized, these stable ACP precursors, acting as high-energy metastable phases, gradually released Ca^{2+} and PO_4^{3-}.[63,64] This localized ionic supersaturation triggered the *in situ* reprecipitation of HA-like minerals within the tubules. Consequently, the CaP synthesized under the regulation of IP6 or H6L in this study demonstrated unique dual advantages: on one hand, the phosphate or carboxyl groups effectively inhibited the rapid aggregation and disordered transformation of ACP by chelating Ca^{2+} ions; on the other hand, the low steric hindrance characteristic of the SOM facilitated the penetration of the stabilized ACP nanoclusters into demineralized dentin tubules and collagen fibrils, thereby promoting dentin repair.[65]

While the aforementioned advantages are significant, it must be objectively acknowledged that the current system has certain limitations. First, the *in vitro* static mineralization model could not fully replicate the complex dynamic microenvironment of the oral cavity, including masticatory stresses, salivary flow, and bacterial colonization. Second, although IP6/CaP demonstrated excellent dentinal tubule occlusion efficacy *in vitro*, the current formulation remained a simplified binary composite. Compared to sophisticated "multifunctional integrated" restorative materials, it lacked inherent antibacterial properties, which are crucial for achieving long-term clinical success in a caries-prone environment. Furthermore, although the acid resistance of the coating was evaluated, the mechanical durability of the mineralized layer under repetitive shear stresses from mastication remained to be quantified. Future directions for improvement should explore the incorporation of synergistic ions (*e.g.*, F^-, Zn^{2+}) or integration with adhesive resins, as well as validation through *in vivo* animal studies, to provide a more substantial basis for the clinical translation of this material.

In summary, owing to its unique molecular structure and strong chelating ability, IP6 can serve as an effective stabilizer for ACP, facilitating the formation of a structurally dense and stable biomimetic mineralized layer. This study not only confirms the significant potential of SOM in regulating biomineralization, but also presents a promising strategy for developing next-generation dentin repair materials.

Conclusions

This study systematically evaluated the biomimetic dentin remineralization performance of three materials: IP6/CaP, H6L/CaP, and CaP. The comprehensive results indicated that the IP6/CaP nanocomposite, regulated by the IP6, effectively stabilized ACP and promoted the formation of a densely structured biomimetic mineralized layer. *In vitro*, it demonstrated excellent rapid tubule-occlusion capability and remarkable acid-resistant stability, with overall performance surpassing that of the H6L/CaP and CaP groups. Thus, IP6/CaP holds considerable promise as a next-generation biomimetic mineralization material for the rapid and durable treatment of dentin hypersensitivity.

Author contributions

Zhenni Liu: conceptualization, methodology, validation, investigation, original draft preparation. Dan Li, Xiujun Shi: data curation. Dongqin Xiao, Feng Shi, Xuwei Luo, Gang Feng: validation, resources. Yonglin Xie, Chengdong Zhang: conceptualization, supervision, validation, editing, project administration.

Conflicts of interest

The authors declare that they have no known competing financial interests or personal relationships that could have appeared to influence the work reported in this paper.

Data availability

Data supporting this study are openly available from the corresponding authors.

Acknowledgements

This study was funded by National Natural Science Foundation of China (82002289), Sichuan Medical Association Medical Research Program (S20250088), Sichuan Provincial Medical Association Young Innovators Project (Q2024026) and Applied Basic Research Program of Nanchong City (25YYJCYJ0054, 25YYJCYJ0060).

References

1 N. X. West, M. Davies, A. Sculean, S. Jepsen, R. Faria-Almeida, M. Harding, F. Graziani, R. G. Newcombe, J. E. Creeth and D. Herrera, *J. Dent.*, 2024, **150**, 105364.

2 G. Campus, R. A. Giacaman and J. C. Carvalho, *Monogr. Oral Sci.*, 2023, **31**, 4–18.

3 A. Ghosh, P. D. Desai, I. Maity and P. Mazumdar, *J. Oral Res. Rev.*, 2025, **17**, 107–112.

4 X. He, S. Yu, H. Wang, Z. Tian, J. Zhang, Y. Zhao, H. Gong, Z. Shi, Z. Cui and S. Zhu, *RSC Adv.*, 2022, **12**, 24288–24300.

5 D. Dai, D. Li and C. Zhang, *Adv. Sci.*, 2024, **11**, 2405763.

6 Z. Liu, D. Yin and C. Deng, *CrystEngComm*, 2026, **28**, 67–77.

7 M. Iafisco, L. Degli Esposti, G. B. Ramírez-Rodríguez, F. Carella, J. Gómez-Morales, A. C. Ionescu, E. Brambilla, A. Tampieri and J. M. Delgado-López, *Sci. Rep.*, 2018, **8**, 17016.

8 S. Shan, Z. Tang, K. Sun, W. Jin, H. Pan, R. Tang, W. Yin, Z. Xie, Z. Chen and C. Shao, *Adv. Healthcare Mater.*, 2024, **13**, 2302418.

9 X. Xu, N. Luo, J. Ru, H. Zeng, X. Liu, S. Tan, F. Chen, B.-Q. Lu and X. Chen, *Adv. Healthcare Mater.*, 2025, **14**, 2405074.

10 A. Indurkar, P. Kudale, V. Rjabovs, I. Heinmaa, Ö. Demir, M. Kirejevs, K. Rubenis, G. Chaturbhuj, M. Turks and J. Locs, *Front. Bioeng. Biotechnol.*, 2024, **11**, 1329752.

11 Y. Pang, C. Fu, D. Zhang, M. Li, X. Zhou, Y. Gao, K. Lin, B. Hu, K. Zhang, Q. Cai, P. Yang, Y. Liu and X. Zhang, *Adv. Funct. Mater.*, 2024, **34**, 2403233.

12 L. Degli Esposti, K. Zheng, A. Piancastelli, A. C. Ionescu, A. Adamiano, A. R. Boccaccini and M. Iafisco, *Ceram. Int.*, 2024, **50**, 593–602.

13 H. Zheng, M. Bian, Z. Zhou, Y. Shi, M. Shen, M. Wang, W. Jiang, C. Shao, R. Tang, H. Pan, J. He, B. Fu and Z. Wu, *ACS Nano*, 2024, **18**, 23537–23552.

14 Y. Feng, D. Wu, J. Knaus, S. Keßler, B. Ni, Z. Chen, J. Avaro, R. Xiong, H. Cölfen and Z. Wang, *Adv. Healthcare Mater.*, 2023, **12**, 2203411.

15 H. Chen, C. Lv, L. Guo, M. Ma, X. Li, Z. Lan, J. Huo, H. Dong, X. Zhu, Q. Zhu, Y. Gu, Z. Liu, J. Liu, H. Chen, X. Guo and J. Ma, *ACS Appl. Mater. Interfaces*, 2022, **14**, 4836–4851.

16 N. Sun, Y. Jia, C. Wang, J. Xia, L. Dai and J. Li, *J. Phys. Chem. Lett.*, 2021, **12**, 10235–10241.

17 G. Toworfe, R. Composto, I. Shapiro and P. Ducheyne, *Biomaterials*, 2006, **27**, 631–642.

18 Q. Yang, W. Zheng, Y. Zhao, Y. Shi, Y. Wang, H. Sun and X. Xu, *Dent. Mater.*, 2024, **40**, 1282–1295.

19 X. Liu, S. Zhang, H. Zheng, M. Bian, L. Qian, W. Zhao, Y. Shi and Z. Wu, *Int. J. Biol. Macromol.*, 2025, **329**, 147720.

20 J. He, J. Yang, M. Li, Y. Li, Y. Pang, J. Deng, X. Zhang and W. Liu, *ACS Nano*, 2022, **16**, 3119–3134.

21 Y. Wang, Y. Zhang, Z. Shen, Y. Qiu, C. Wang, Z. Wu, M. Shen, C. Shao, R. Tang, M. Hannig, B. Fu and Z. Zhou, *Adv. Healthcare Mater.*, 2024, **13**, 2400102.

22 S. Tan, S. Chen, Y. Wang, F. Wu, Y. Shi, J. Wang, Y. Du and S. Zhang, *Dent. Mater.*, 2020, **36**, 816–825.

23 J. Huang, *J. Phys.: Conf. Ser.*, 2025, **3112**, 012039.

24 W. Gao, C. Wan, Z. Han, C. Li, Y. Zhao and L. Liu, *Int. J. Nanomed.*, 2025, **20**, 9981–9998.

25 J. Wang, Z.-J. Lin, Y.-C. Ou, Y. Shen, R. Herchel and M.-L. Tong, *Chem.–Eur. J.*, 2008, **14**, 7218–7235.

26 A. Wong and J. Czernuszka, *J. Mater. Sci.: Mater. Med.*, 1993, **4**, 107–110.

27 W. Zhao, Z. Wang, Z. Xu and N. Sahai, *Phys. Chem. Chem. Phys.*, 2018, **20**, 13047–13056.

28 A. Indurkar, R. Choudhary, K. Rubenis, M. Nimbalkar, A. Sarakovskis, A. R. Boccaccini and J. Locs, *ACS Omega*, 2023, **8**, 26782–26792.

29 M. S. Strelova, E. N. Danilovtseva, S. N. Zelinskiy, V. A. Pal'shin and V. V. Annenkov, *Langmuir*, 2024, **40**, 18016–18027.

30 D.-Y. Liu, J. Wu, H.-Y. Zhou, J.-X. Lv, K.-Z. Cai and C.-B. Tang, *Chem.-Biol. Interact.*, 2024, **387**, 110818.

31 G. Asensio, M. Martín-del-Campo, R. A. Ramírez, L. Rojo and B. Vázquez-Lasa, *Pharmaceutics*, 2023, **15**, 339.

32 D. Xiao, T. Guo, F. Yang, G. Feng, F. Shi, J. Li, D. Wang, K. Duan and J. Weng, *Ceram. Int.*, 2017, **43**, 1588–1596.

33 V. W. H. Leung and B. W. Darvell, *J. Dent.*, 1997, **25**, 475–484.

34 M. Chaari, M. Megdiche and M. Arous, *RSC Adv.*, 2026, **16**, 2133–2148.

35 D. Xiao, X. Zhou, H. Li, Y. Fu, K. Duan, X. Lu, X. Zheng and J. Weng, *J. Eur. Ceram. Soc.*, 2015, **35**, 1971–1978.

36 G. Dave and H. Modi, *J. Food Meas. Char.*, 2018, **12**, 2202–2208.

37 W. Querido, N. a. Shanas, S. Bookbinder, M. C. Oliveira-Nunes, B. Krynska and N. Pleshko, *Analyst*, 2020, **145**, 764–776.

38 D. Xiao, Z. Tan, Y. Fu, K. Duan, X. Zheng, X. Lu and J. Weng, *Ceram. Int.*, 2014, **40**, 10183–10188.

39 H. Ping, H. Xie, Y. Wan, Z. Zhang, J. Zhang, M. Xiang, J. Xie, H. Wang, W. Wang and Z. Fu, *J. Mater. Chem. B*, 2016, **4**, 880–886.

40 V. Bystrov, A. Bystrova and Y. Dekhtyar, *Adv. Colloid Interface Sci.*, 2017, **249**, 213–219.

41 E. Gachon and P. Mesquida, *ACS Nano*, 2021, **15**, 9820–9826.

42 S. Tan, S. Chen, Q. Lei and D. Ma, *Dent. Mater.*, 2023, **39**, 260–274.

43 N. Luo, B.-Q. Lu, Y.-W. Deng, H. Zeng, Y. Zhang, J.-Y. Zhan, X.-C. Xu, G.-Z. Cao, J. Wen, Z. Zhang, X.-P. Feng, X. Jiang, F. Chen and X. Chen, *Nat. Commun.*, 2025, **16**, 58.

44 W.-C. Chen, C.-H. Chen, J.-C. Kung, Y.-C. Hsiao, C.-J. Shih and C.-S. Chien, *Materials*, 2013, **6**, 5335–5351.

45 H. Yu, Y. Hou, W. Zhou, L. Sun, L. Guo, N. Wang, P. Pan, J. Su and J. Chen, *Nano Today*, 2026, **67**, 102958.

46 A. George and A. Veis, *Chem. Rev.*, 2008, **108**, 4670–4693.

47 B. Palazzo, D. Walsh, M. Iafisco, E. Foresti, L. Bertinetti, G. Martra, C. L. Bianchi, G. Cappelletti and N. Roveri, *Acta Biomater.*, 2009, **5**, 1241–1252.

48 J. Chen, G. Xian, Z. Xiao, F. Ge, S. Yuan, B. Li, X. Liang, Z. Cai, N. Zhang, L. Zhang, Z. A. Li, L. Deng, C. Zeng and D. Xie, *Bioact. Mater.*, 2026, **56**, 260–276.

49 F. Nudelman, K. Pieterse, A. George, P. H. H. Bomans, H. Friedrich, L. J. Brylka, P. A. J. Hilbers, G. de With and N. A. J. M. Sommerdijk, *Nat. Mater.*, 2010, **9**, 1004–1009.

50 W. Zhu, C. Mi, R. Zhou, H. Guo, S. Bao, K. Liang, J. Li and P. Ji, *Int. J. Biol. Macromol.*, 2025, **315**, 144584.

51 Y. Chen, X. Yang, S. Zhang, H. Wang, H. Xie and C. Chen, *Dent. Mater.*, 2026, **42**, 126–137.

52 G. Williams and J. D. Sallis, *Calcif. Tissue Int.*, 1982, **34**, 169–177.

53 J. F. R. Oliveira, A. J. S. Rocha, U. A. d. O. Filho, F. R. S. Silveira, G. M. L. Dalmonico and E. A. dos Santos, *J. Non-Cryst. Solids*, 2025, **668**, 123756.

54 L. Degli Esposti, A. Adamiano, D. Siliqi, C. Giannini and M. Iafisco, *Bioact. Mater.*, 2021, **6**, 2360–2371.

55 V. Uskoković, S. Marković, L. Veselinović, S. Škapin, N. Ignjatović and D. P. Uskoković, *Phys. Chem. Chem. Phys.*, 2018, **20**, 29221–29235.

56 H. Xie, J. Sun, F. Xie and S. He, *RSC Adv.*, 2023, **13**, 11733–11741.

57 L. Zhu, W. Liu, Y. Zhang, Z. Wu, Y. Wang, Y. Xu, H. Zheng, H. Zhang, M. Yu, X. Jin, Z. Wang, Z. Zhou and B. Fu, *Adv. Sci.*, 2025, **12**, 2501340.

58 B. Han, Y. Song, S. Wang, T. Yang, Z. Sun, A. Wang, M. Jin, Z. Yang, X. Wang and F. Liang, *Adv. Funct. Mater.*, 2025, **35**, 2412954.

59 J. R. Jones, *Acta Biomater.*, 2013, **9**, 4457–4486.

60 Y.-C. Chiang, H.-P. Lin, H.-H. Chang, Y.-W. Cheng, H.-Y. Tang, W.-C. Yen, P.-Y. Lin, K.-W. Chang and C.-P. Lin, *ACS Nano*, 2014, **8**, 12502–12513.

61 E. A. Abou Neel, A. Aljabo, A. Strange, S. Ibrahim, M. Coathup, A. M. Young, L. Bozec and V. Mudera, *Int. J. Nanomed.*, 2016, **11**, 4743–4763.

62 R. Wang, Q. Wang, X. Wang, L. Tian, H. Liu, M. Zhao, C. Peng, Q. Cai and Y. Shi, *Biomater. Appl.*, 2014, **29**, 268–277.

63 R.-H. Lai, P.-J. Dong, Y.-L. Wang and J.-B. Luo, *Chin. Chem. Lett.*, 2014, **25**, 295–298.

64 J. Luo, S. Qiu, X. Zhou, R. Lai, P. Dong and X. Xie, *Colloids Surf., A*, 2014, **444**, 81–88.

65 H. Huang, M. Fan, A. Yang, D. Chang, J. Li, L. Yang, X. Li, M. Wang, P. Zheng, T. Guo and J. Weng, *Appl. Mater. Today*, 2024, **38**, 102171.